Journal of
Instrumentation

PAPER • OPEN ACCESS

Performance of a $CeBr_3$ scintillator coupled to a photomultiplier tube with an active voltage divider under high bremsstrahlung fluences

Published by IOP Publishing for Sissa Medialab

Received: *October 1, 2025*
Accepted: *November 6, 2025*
Published: *November 21, 2025*

Performance of a $CeBr_3$ scintillator coupled to a photomultiplier tube with an active voltage divider under high bremsstrahlung fluences

I. García Rivas,[a,b,*] **A. Fernández Prieto**,[a] **P. Vázquez Regueiro**,[a] **D. García Fernández**,[b] **T. Kögler**,[c,d] **K. Römer**[e] **and F. Hueso-González**[f]

[a] *Instituto Galego de Física de Altas Enerxías (IGFAE), University of Santiago de Compostela (USC), Rúa de Xoaquín Díaz de Rábago, s/n, Santiago de Compostela, Spain*

[b] *TripleAlpha Innovation, C/ José Villar Granjel 22, Santiago de Compostela, Spain*

[c] *OncoRay — National Center for Radiation Research in Oncology, Medical Faculty and University Hospital Carl Gustav Carus, TUD Dresden University of Technology, Helmholtz-Zentrum Dresden-Rossendorf, Fetscherstr. 74, Dresden, Germany*

[d] *Institute of Radiooncology — OncoRay, Helmholtz-Zentrum Dresden-Rossendorf, Bautzner Landstraße 400, Dresden, Germany*

[e] *Institute of Nuclear Physics, Helmholtz-Zentrum Dresden-Rossendorf, Bautzner Landstraße 400, Dresden, Germany*

[f] *Instituto de Física Corpuscular (IFIC), CSIC-UV, C/ Catedrático José Beltrán, 2, Paterna, Spain*

E-mail: irisgarcia.rivas@usc.es

Abstract: Proton therapy lacks a standard method to verify the proton range during the treatments in the clinical routine. In this context, the monitoring of prompt γ-rays in a coaxial geometry using a compact detector based on a $CeBr_3$ scintillator coupled to a commercial photomultiplier tube (PMT) could lead to the identification of proton range deviations. Such detection system could be easily integrated in every treatment room. Although measuring in this geometry profits from an advantageous solid angle, the detector is also exposed to an extreme γ-ray rate, of up to 10 Mcps. In this work, we present the first experimental performance evaluation for the proposed detector by irradiating it at very high bremsstrahlung rates at the γELBE facility. Using a customized active voltage divider to supply voltage to the PMT, the detection system was able to sustain a photon rate higher than 12 Mcps without dead time while keeping gain drifts below 15 % in the best configuration, and to achieve a sub-nanosecond time resolution.

Keywords: Gamma detectors; Instrumentation for hadron therapy; Analogue electronic circuits; Data processing methods

*Corresponding author.

https://doi.org/10.1088/1748-0221/20/11/P11016

2025 JINST 20 P11016

Contents

1 Introduction

Proton therapy is one modality of radiation therapy for cancer treatment. Accelerated protons are responsible for delivering the dose to the tumor. The main advantage of proton therapy compared to conventional X-ray radiotherapy is that the ionization maximum (Bragg peak) is located close to the particle range [1], thus allowing more dose conformity and preventing the irradiation of normal tissue behind the tumor [1].

Despite its potential for reducing radiation toxicity, proton therapy lacks a standardized method to verify the proton range *in vivo* today [2]. Due to range uncertainties, conservative safety margins are applied in the clinical practice to ensure tumor coverage. To fully exploit the potential that protons can offer, it would be highly desirable to reduce safety margins based on a proton range verification system [3].

2025 JINST 20 P11016

The measurement of the prompt γ-rays, a by-product of the irradiation of the tissue with protons, constitutes a way for real-time range verification, since their emission profile correlates strongly with the Bragg peak. However, this measurement is challenging because of the large radiation background produced during the treatment together with the prompt γ-rays. Neutrons emitted due to reactions of the protons with nuclei across the beam path play an important role as background source. In contrast to protons, their range is usually large enough to exit the patient, and they may interact with the surrounding materials (such as the couch, room walls, etc.), leading to secondary γ-rays that do not provide valuable information on the proton range. These two sources of γ-rays result in an energy spectrum covering up to ~12 MeV [4].

Most attempts [3, 5–7] to monitor prompt γ-rays for proton range verification rely on collimated γ-ray cameras, which are routinely used for imaging in nuclear medicine. However, these must be newly designed with much thicker and dense collimators to absorb their high energies [1, 8]. This complicates the integration of the camera into the rotating gantry system, especially in compact rooms. To avoid the use of these heavy collimators, a new measurement strategy is being developed: the Coaxial Prompt γ-ray Monitoring. Prompt γ-rays are measured with a single fast scintillation detector positioned coaxially to the beam and behind the irradiated area, as described in [9].

In this innovative geometrical arrangement, proton range deviations can be derived from changes in the number of prompt γ-rays detected per proton with respect to the expected value. The latter can be derived from Monte Carlo simulations of the nominal scenario [9]. The former relies on the counting of γ-rays interacting with a scintillation crystal and depends on the solid angle: the deeper the protons penetrate, the closer the distance between the generated prompt γ-rays and the detector, and thus the higher the number of prompt γ-rays detected.

A typical treatment plan in pencil-beam scanning consists of two fields (gantry angles), each field consisting of 1000 spots. Each spot contains between 10 and 100 million protons. On average, between 1 and 10 million γ-rays are emitted in 4π per spot [10], at a rate of 1.2 billion γ-rays per second (~2 nA proton beam current). In coaxial geometry, considering a ⌀1" × 1" thickness scintillator and assuming a solid angle coverage of 2 % (4.5 cm distance between Bragg peak and detector) and crystal interaction efficiency of 40 % (see eq. (5) in [9]), up to ~10 million γ-rays per second (including both prompt and background) would interact with this detector. Hence, the equipment has to be able to maintain a stable signal in such challenging conditions [10, 11].

The sensitivity of the coaxial method was first evaluated in a theoretical study [9] for a $LaBr_3$ scintillation crystal. In that study, considering the irradiation of an homogeneous water phantom with a 125 MeV proton beam at a clinical current of 2 nA, a change in the count rate of ~3 % for range deviations of 1 mm was reported. More recently, Monte Carlo simulations of the irradiation of an anthropomorphic phantom support that a $CeBr_3$ fast scintillation detector placed in coaxial geometry is sensitive to changes in the proton range [12]. This encourages further investigations to experimentally confirm these findings.

In the present work, we undertake the first step in the experimental implementation of the theoretical method presented in [9]. We develop and test a detector prototype under relevant clinical-like conditions at Electron Linear accelerator of high Brilliance and low Emittance (ELBE) at Helmholtz-Zentrum Dresden-Rossendorf (HZDR) [13]. The main goal of this work is to evaluate the performance of the proposed detector to operate under challenging γ-ray rates in the Mcps range, similar to those expected in a clinical proton treatment. This includes the investigation of the maximal γ-ray rate that the detection system is able to withstand, evaluating possible instabilities of the signal gain and baseline. The linearity of the response of the detector after signal reconstruction with the incident γ-ray rate will

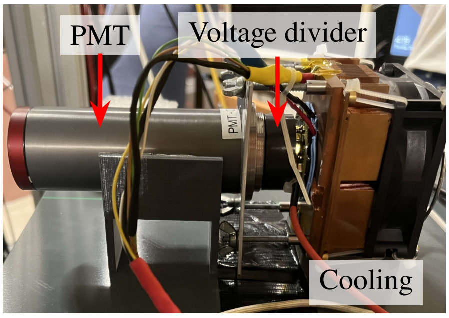

(a) View of the detector parts (PMT, active voltage divider and cooling) from its lateral face.

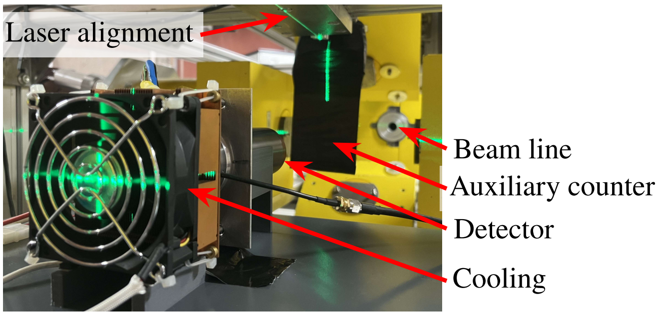

(b) Picture of detector alignment with respect to beam axis and of the auxiliary plastic scintillator (reference counter) between detector and beam.

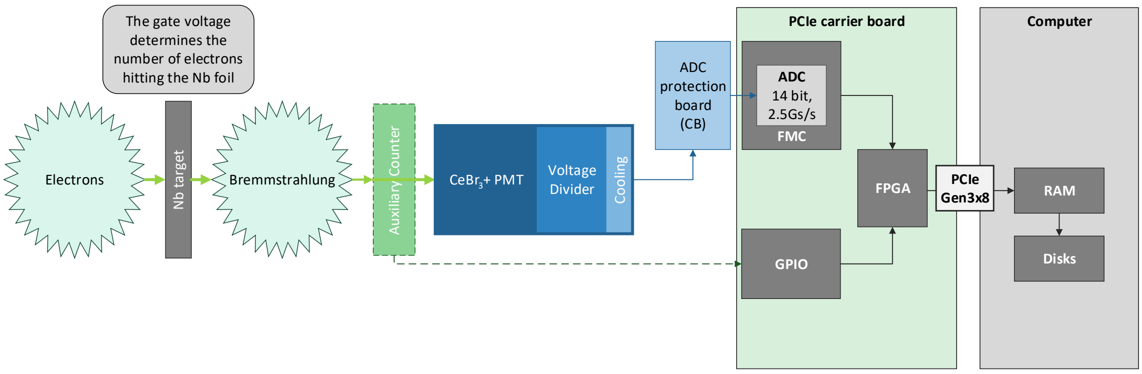

(c) Setup scheme: after bremsstrahlung is produced (left), the bremsstrahlung photons interact with the auxiliary counter and the detector. The detector signals are digitized at 2.5 GSPS with a 14-bit Analog to Digital Converter (ADC) after being reshaped in the ADC protection board. The signals from the auxiliary counter are converted to status bits in the General Purpose Input Output (GPIO) board. Finally, all data are sent by the Field Programmable Gate Array (FPGA) to the computer memory as described in [14].

Figure 1. Experimental setup.

be also investigated, thus assessing the limitations of the reconstruction method. The influence of the incident γ-ray rate in the energy and time resolution of the detector will be characterized. Finally, the suitability of the developed system as coaxial monitor in a proton therapy facility will be discussed.

2 Materials

2.1 Coaxial detector

Our setup comprises a cylindrical $\varnothing 1'' \times 1''$ $CeBr_3$ crystal (scintillation light wavelength ~380 nm and exponential decay constant of 25 ns [15]) coupled to an R13408-100 photomultiplier tube (PMT) from Hamamatsu Photonics K. K. (Hamamatsu City, Japan) operated with negative polarity. The detector arrangement is shown in figure 1(a).

2025 JINST 20 P11016

As the detector must be able to cope with high γ-ray count rates [9], a customized fully active voltage divider was designed and manufactured [16]. With this voltage divider, the voltages of the dynodes are stabilized by a cascade of P-channel MOSFET transistors and Zener diodes [16].

To provide the high voltage (HV) to our detector, we use a C12766-12 power supply module from Hamamatsu Photonics which can provide a voltage up to -1500 V and a maximal output current of 30 mA. This high current output is needed when high γ-ray rates hit the scintillation crystal. The resulting high currents through the transistors increase their temperature, which is dissipated with an in-house cooling system based on a metal block attached to the transistors coupled to a fan (figure 1(b)).

A fast plastic polyvinyltuolene (PVT) scintillator with dimensions $150 \times 100 \times 10\,\mathrm{mm}^3$ was deployed as a reference beam monitor for this experiment.

2.2 Readout electronics

The readout electronics are based on the dead-time-free and trigger-less data acquisition system presented in [14], specifically developed for this application. Data are digitized at 2.5 GSPS with a DC-coupled 14-bit dual-channel Analog to Digital Converter (ADC) AD9689 from Analog Devices (Wilmington, MA, U.S.A.). The ADC is supplied on an FPGA Mezzanine Card (FMC) card SFMC01 on top of a Peripheral Component Interconnect Express (PCIe) Gen3×8 carrier SIS1160 by Struck Innovative Systeme (Hamburg, Germany) [14]. This chain is designed to continuously digitize and stream the signals to a computer in the course of an irradiation.

In order to protect the ADC from pulses exceeding its current limit, the anode signal of the PMT was adapted to fit the ADC dynamic range with an intermediate conditioning board (CB). Three CBs with different inverting gains (0.3 for CB1, 1 for CB2 and 3 for CB3) were manufactured. The PMT HV was varied from -1000 to -1500 V and all possible combinations HV-CB were explored to select the most suitable for further experiments in a proton therapy facility.

The $CeBr_3$ detector analog signal as well as the plastic detector trigger output were recorded. The main detector data was digitized with one channel of the 14-bit ADC, whereas the auxiliary detector trigger was plugged on to a General Purpose Input Output (GPIO) channel and stored as a logical signal (1 bit). In order to perform a continuous acquisition, the Field Programmable Gate Array (FPGA) streamed both data to the Random-Access Memory (RAM) of the computer in 16-bit words, where they were later stored as raw binary files into the Solid State Drive (SSD). A schematic representation of the acquisition chain is depicted in figure 1(c).

2.3 Experimental setup

The whole detection chain was tested at γELBE [13]. This accelerator was set to provide a continuous-wave electron beam of 13 MeV (total energy) with a micro-bunch repetition rate $f_{\mu\mathrm{b}} = 13$ MHz, corresponding to a micro-bunch period $T_{\mu\mathrm{b}}$ of 76.9 ns duration. The electrons are focused to a diameter below 2 mm and shot onto a 2 µm thick niobium foil. Bremsstrahlung with a continuous energy distribution up to 12.5 MeV is instantaneously emitted as a result of the deflection of the electrons in the electric field of the niobium nucleus [13]. In each micro-bunch, the bremsstrahlung photons (BPs) are emitted within a time window of 5 ps [13]. This time window is not relevant for the clinical scenario, since it is defined by the micro-bunch repetition rate $f_{\mu\mathrm{b}}$ of this particular electron accelerator. In the clinical setting, the micro-time structure of the emitted protons determines the arrival time of the prompt γ-rays. This micro-time structure typically ranges from 250 ps to 2 ns depending on the

Table 1. Comparison of γELBE bremsstrahlung characteristics and the prompt γ-rays produced in a proton therapy irradiation.

	Clinical	γELBE
Accelerated particle	Proton	Electron
γ-ray energy spectrum	Up to ~12 MeV	Up to 12.5 MeV[a]
γ-ray rate in the detector	0.1 - 10 Mcps[b]	-
Accelerator radiofrequency	106 MHz[c]	1.3 GHz[d]
Micro-bunch repetition	106 MHz[c] (9.4 ns)	13 MHz[a] (76.9 ns)
Micro-bunch duration	250 ps – 2 ns[c]	~5 ps
Macro-pulse structure	ms spot duration	Continuous[a]

[a]Settings in present work.

[b]Expected values from [9].

[c]Isochronous cyclotrons of type C230, from [10].

[d]Substructure at 260 MHz [13] due to an intermediate buncher.

energy for isochronous cyclotrons [17]. After accounting for the spread introduced by the different proton transit times in the target [18], the time window of prompt γ-ray detection is ~2 ns for all energies [8]. A comparison between the characteristics of the BPs produced in γELBE (as set up in this experiment) and the prompt γ-rays expected in the clinical setting are summarized in table 1.

Using this bremsstrahlung beam, we aimed to emulate the prompt γ-rays that are produced during a proton therapy treatment. Despite the differences between both scenarios, it let us achieve high rates in the detector with an energy spectrum similar to that emitted in the clinical setting, so the detector capability to operate under clinical-like scenarios can be evaluated. To emulate the geometry described in [9], the detector was placed directly in front of the beam (see figure 1(b)).

Finally, a γ-ray emitting radioactive source was placed next to the detector to use its characteristic emission as energy reference. For configurations at HV = −1200 and −1300 V, a ^{22}Na source (positron emitter with a characteristic γ-ray emission at 1275 keV) was used. With this nuclide, the detection of 511 keV photons is more likely than the detection of 1275 keV photons, and since our low energy detection limit was precisely about 511 keV, it was preferable to use another nuclide with characteristic emission at higher energies for reference purposes. For this reason, we used a ^{137}Cs source that undergoes β^--decays with subsequent γ-ray emission at 662 keV for the rest of the measurements.

2.4 Fluence of bremsstrahlung photons

The rate of BPs coming from the beam was set via an indirect magnitude, the so-called gate voltage, denoted as U_{GV}, which corresponds to the voltage applied to the accelerator gate that releases electrons to the cavities. Consequently, the U_{GV} controls the number of electrons that eventually produce bremsstrahlung at the Nb film, and hence sets the BP rate, but the relationship between U_{GV} and emitted BP rate is not calibrated in advance. We varied this voltage in order to record in the detector a BP rate between 1 and 10 Mcps. This corresponds to an average BP fluence from $5{\cdot}10^5$ to $5{\cdot}10^6\,\mathrm{cm}^{-2}\mathrm{s}^{-1}$ through the $CeBr_3$ detector front face.

2025 JINST 20 P11016

Although all measurements were conducted with a reference fluence monitor placed between the beam exit window and the detector under test (as shown in figure 1(a)), the information provided by this counter was not used for the analysis because of a misconfiguration of the GPIO board.

3 Methods

3.1 Data acquisition

The data acquisition was set to start before the beam was turned on; in this way, each dataset contains a time interval with only radioactive source data and another one with both radioactive source and BPs, allowing us to observe the change between low and high detector load. For the purpose of the current analysis, we present the information corresponding to the first 2 seconds of the irradiation. Since in the clinical setting with pencil-beam scanning, protons are delivered in spots of few milliseconds [10], measuring the detector response during 2 s is sufficient to investigate detector short-term stability.

3.2 Digital signal processing

Signal processing is performed offline, once the data are stored on disk. An important part of this analysis is the identification of individual signals corresponding to BPs releasing their energy in the detector in a context where pile-up effects are present, specially at high radiation rates. To this extent, we have devised a customized signal identification and pile-up deconvolution algorithm that distinguishes signals by template matching and further reconstructs the energy of the individual incoming photons.

Templates are generated by averaging digitized signals of selected scintillation events after horizontal alignment (so that sample 20 matches 50% of the signal maximum) and vertical normalization (maximum is at 1). Then, the normalized cross correlation between the template and the raw data is calculated point by point throughout the whole measurement waveform. The normalized cross correlation metric lets us measure the linear association between two variables by eliminating the dependence on the amplitude of the signals being compared [19]. The chosen template length is 76 ns, which corresponds to 190 points at a sampling rate of 0.4 ns, representing almost one period $T_{\mu\text{b}}$. The templates are generated independently for each dataset.

Let x be an array containing the 190 template points, w an array with the whole digitized measurement, and y_i an excerpt of w between samples $[i-20, i+169]$, all arrays with the same time steps. Then the correlation at sample i between x and y_i is calculated by:

$$\operatorname{cor}(i) = \frac{\operatorname{cov}(x, y_i)}{\sqrt{\operatorname{var}(x) \cdot \operatorname{var}(y_i)}} \tag{3.1}$$

A leading edge threshold algorithm is applied on the resulting correlation waveform cor. We set an empirical threshold for the event identification of $\operatorname{cor}(i) > 0.85$. In the contiguous region of samples j where this condition is satisfied, we search for the sample $j_{\max}$ where $\operatorname{cor}(j)$ is maximum (an interpolation is performed for subsample accuracy). The leading edge search for the next event is continued after this region j.

The calibrated absolute timestamp t of the event is calculated as $t = j_{\max} \cdot 0.4$ ns. The relative time within a $T_{\mu\text{b}}$ period, i.e. with respect to the previous closest micro-bunch $t_{\mu\text{b}}$, yields:

$$t - t_{\mu\text{b}} \equiv t - \lfloor t/T_{\mu\text{b}} \rfloor \cdot T_{\mu\text{b}} \tag{3.2}$$

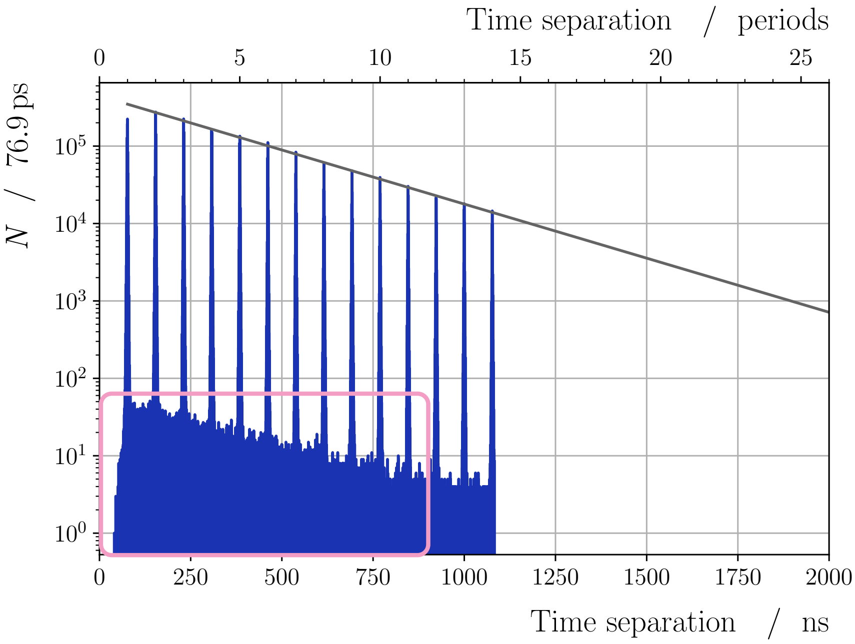

Figure 2. Time difference measured experimentally between consecutive (detected) events at the ELBE bremsstrahlung beam. The micro-bunch structure (13 MHz) due to pulsed emission of the BPs can be observed as sharp peaks. The average structure follows an exponential distribution. This dataset was measured at −1000 V (CB3), with a resulting interacting rate of $\dot{N}_{\text{int}} = (3.22 \pm 0.07)$ Mcps (fit) and a recorded rate of $\dot{N}_{\text{rec}} = (2.84 \pm 0.06)$ Mcps. The background area indicated with the pink rectangle corresponds to the contribution of the radioactive source and accelerator dark current (4 orders of magnitude smaller).

Note that this is a surrogate of the previous electron micro-bunch emission time, the actual phase (transit time offsets) is not known.

Since the template is normalized to unity, the amplitude in ADC counts of the identified event is also derived from the covariance and the variance:

$$\text{amplitude} = \frac{\text{cov}(x, y_{j_{\max}})}{\text{var}(x)} \tag{3.3}$$

The derived correlation and amplitude are insensitive to constant baseline offsets. In case that the event happens on top of the exponential decay of a previous event, the algorithm will return biased results, since the offset is not constant. However, the bias will be moderate, since the signals have a typical rise time of <10 ns, much smaller than the decay time of 150 ns, i.e. at first order, the baseline offset is constant within the 10 ns of largest interest for the template matching.

Finally, a histogram of the amplitudes is fitted to derive a calibration curve E(amplitude) between ADC counts and energy using the source's characteristic emission photopeak.

3.3 Bremsstrahlung photon rate estimation

The fluence of BPs being emitted is changed by varying the U_{GV} (see section 2). Since the BP emission follows a micro-time structure given by $f_{\mu\text{b}}$, the same structure is present in the distribution of the time difference between signals, as can be seen in figure 2. In this figure, the secondary horizontal axis on the top of the image shows the time difference in number of periods $T_{\mu\text{b}}$ of 76.9 ns duration.

2025 JINST 20 P11016

The continuum in the figure (pink rectangle) comprises γ-rays from the radioactive source, BPs from the beam dark current at 260 MHz ($_{\text{dark}}$BPs) and other background sources. These time separations occur at a frequency approximately four orders of magnitude lower than that of the BP peaks at multiples of 76.9 ns. Therefore, in the following, we refer to the micro-bunch-correlated events simply as BPs, while acknowledging the minor contribution from γ-rays.

If two or more BPs from the same electron micro-bunch (emitted within a time window of 5 ps) interact with the detector, they will generate a so-called sum event, because the number of produced scintillation photons is proportional to the sum of the energies of the individual BPs. These events result in only one signal, so the corresponding peak in figure 2 at $(t - t_{\mu\text{b}} = 0)$ ns is not visible.

On the other hand, BPs coming from consecutive bunches generate pile-up pulses, since the time difference between bunches (76.9 ns) is lower than the characteristic shaping time of the deployed CB (150 ns, much larger than the intrinsic 25 ns of a $CeBr_3$ crystal). Pile-up events can also be a result of $_{\text{dark}}$BPs or γ-rays from the radioactive source that interact in the crystal within the 150 ns following a previous interaction. Given that the selected template length for the present analysis is 76 ns, about 30 % of the signals whose relative time difference is lower than this length would not be correctly deconvoluted, and this contributes to the loss of events between the peaks corresponding to the first and second period in figure 2. In a general sense, the deconvolution capability for piled-up signals closer than 76.9 ns strongly depends on the amplitude to noise ratio of the involved waveform.

An example of the digitized raw waveform is depicted in figure 3. Blue lines indicate the periods $T_{\mu\text{b}}$ of 76.9 ns duration, evidencing signal synchrony with $f_{\mu\text{b}}$. In this experiment, 16 384 ADC counts (14-bit ADC dynamic range) corresponded to 1.7 V_{pp}. The deconvoluted amplitudes are indicated with violet markers. Markers are relative to the left vertical axis (ADC counts). Baseline subtraction is not necessary for the deconvolution (the deconvolution algorithm is baseline independent). The slight offset of the markers vertical position with respect to the pulse maximum is caused by a varying baseline, which results from load drifts: high currents in the CB generate a baseline undershoot that recovers after load reduction, as observed in the pink rectangle. At 2800 ns (~7250 ADC sample points) a signal is not identified by the algorithm. At 1600 ns (~4200 ADC sample points) one high amplitude signal is cropped by the CB to avoid damaging the ADC.

When estimating the rate of BPs interacting with the detector, the contribution of the sum events must be taken into account. To this end, let $\dot{N}_{\text{int}}$ be the average rate at which the BPs interact with the detector. The time difference between consecutive events follows an exponential distribution (see figure 2) due to Poisson statistics [20]. Hence, $\dot{N}_{\text{int}}$ can be obtained from the fit of the histogram (with bin width bw) of time differences Δt between consecutive events:

$$N(\Delta t_i)/\text{bw} = N_0/\text{bw} \cdot e^{-\dot{N}_{\text{int}} \cdot \Delta t_i} \tag{3.4}$$

where $N(\Delta t_i)$ are the histogram bin contents and N_0 is not related with the photon rate. This equation is valid if the fitting range includes several periods $T_{\mu\text{b}}$.

Let $\dot{N}_{\text{rec}}$ be the average rate of recorded signals blind to sum events. For its estimation, let P_i be the probability that i BPs from the same electron bunch interact with the detector. P_i is described by the Poisson distribution:

$$P_i = P_i(i, \lambda) = \frac{\lambda^i \mathrm{e}^{-\lambda}}{i!} \tag{3.5}$$

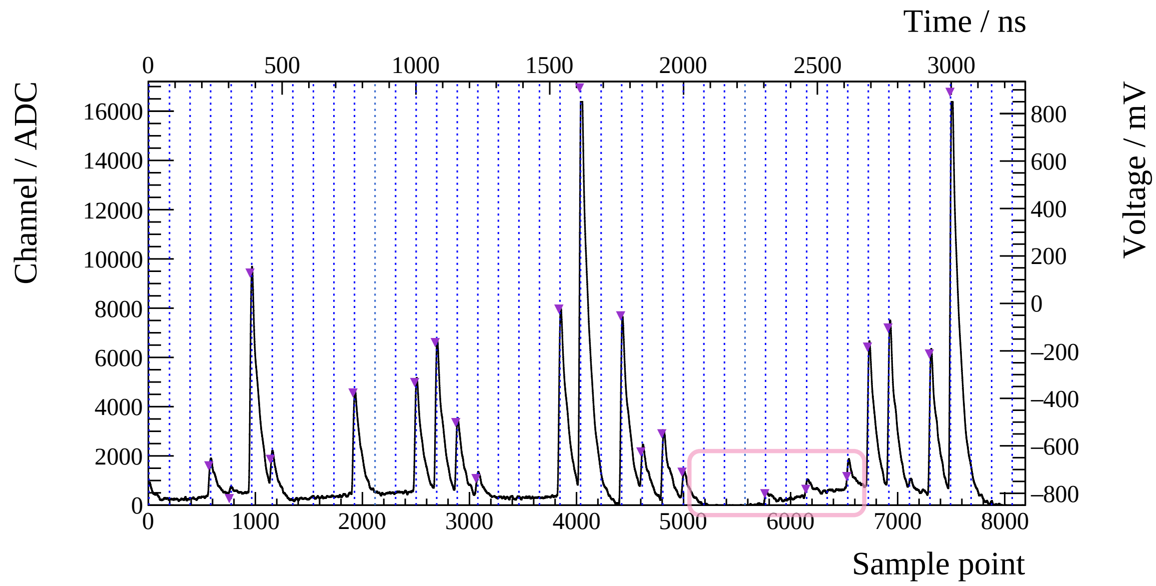

Figure 3. Raw data at moderate BP fluence (~3 Mcps). The blue lines indicate the accelerator micro-bunch repetition rate $f_{\mu b}$ of 13 MHz. Individual signals are deconvoluted and identified with violet markers. The part of the waveform enclosed by the pink rectangle suffers from a baseline undershoot after a load reduction.

where λ is the average number of BPs interacting with the detector per electron micro-bunch:

$$\lambda = \frac{\dot{N}_{\mathrm{int}}}{f_{\mathrm{ELBE}}} = \sum_{i=0}^{\infty} i \cdot P_i \tag{3.6}$$

Notice that in the range of gate voltages that we configure, $O_\lambda(1)$ indicating that the probability of detecting zero BPs for one electron micro-bunch is not negligible.

For sum events, since only one event is identified, only the contribution of one of the BPs is included in $\dot{N}_{\mathrm{rec}}$. Considering the probabilities P_i given by eq. (3.5), the number of unrecorded BPs is given by:

$$\sum_{i=2}^{\infty} (i-1)\, P_i = \sum_{i=2}^{\infty} i \cdot P_i - \sum_{i=2}^{\infty} P_i = \lambda - (1 - P_0) \tag{3.7}$$

And $\dot{N}_{\mathrm{rec}}$ can be then estimated:

$$\dot{N}_{\mathrm{rec}} = \dot{N}_{\mathrm{int}} - f_{\mathrm{ELBE}} \sum_{i=2}^{\infty} (i-1)\, P_i = f_{\mathrm{ELBE}} (1 - P_0) = f_{\mathrm{ELBE}} (1 - \mathrm{e}^{-\dot{N}_{\mathrm{int}}/f_{\mathrm{ELBE}}}) \tag{3.8}$$

This value can be compared with the quotient $\Delta N_{\mathrm{rec}}/\Delta t$ of the total number of events ΔN recorded in a time window Δt.

The fraction of simultaneous events which lead to sum events is given by:

$$\frac{N_{\mathrm{sum}}}{N_{\mathrm{int}}} = \frac{1 - P_0 - P_1}{1 - P_0} \tag{3.9}$$

To conclude, in order to establish a relationship between U_{GV} and the BP rate, a fit to a grade 3 polynomial curve is performed:

$$\dot{N} = a + b \cdot U_{\mathrm{GV}} + c \cdot (U_{\mathrm{GV}})^2 + d \cdot (U_{\mathrm{GV}})^3 \tag{3.10}$$

with different coefficients a, b, c and d for $\dot{N}_{\mathrm{int}}$ and $\dot{N}_{\mathrm{rec}}$.

3.4 Anode current

Since one of the goals of this experiment is to find the operation limit in terms of BP interaction rates for the detector, the current flowing through the PMT anode is a relevant quantity because it is proportional to the light produced in the scintillation crystal and thus to the energy deposited by the BPs in the detector.

The anode current is obtained by integrating the detector output signal. A gain correction factor (see section 2.2) is applied in the calculation to account for the amplification introduced by the CBs. This correction is approximate, as the CB clips signals exceeding a certain limit. In addition, absolute current values from the HV supply are monitored, although with limited temporal resolution due to the low sampling frequency (0.5–1 Hz).

At γ-ray rates expected in a clinical scenario, the predicted anode current is in the mA range. These high currents may damage the PMT on the long-term, so we also focus on studying potential deterioration in the PMT output.

3.5 Gain and baseline drifts

Ideally, the rate of the incoming γ-ray should not change the PMT or CB gain, nor the signal baseline. However, the signal baseline and the system gain system vary during the operation time if the current flowing through the PMT is high (in the mA range) [16]. Therefore, gain drifts are expected [4] and should be studied.

We focus on quantifying relative gain shifts within a measurement by using the characteristic signature of the full photoabsorption of the radioactive sources described in section 2 as reference.

Time filters are applied to isolate the events from the radioactive source (with a contribution of the ${}_{\text{dark}}$BP signals) from the beam BPs. Then, an energy spectrum is generated and the position of the characteristic peak is obtained by performing a Gaussian fit with $x \equiv E$:

$$f(x) = \frac{1}{\sqrt{2\pi\sigma^2}} e^{\frac{(x-\mu)^2}{2\sigma^2}} \tag{3.11}$$

Then, relative gain drifts Δg are obtained as follows:

$$\Delta g = \frac{\mu_{\text{off}} - \mu_{\text{on}}}{\mu_{\text{off}}} \tag{3.12}$$

where μ_{off} and μ_{on} indicate the centroids of the fits when the beam is switched off and on, respectively.

Baseline drifts are studied by averaging areas of the waveform without events as a function of time.

3.6 Energy resolution

The characteristic photopeak energy E_γ of the radioactive source in the energy spectrum serves to determine the energy resolution R_{E} as Full Width at Half Maximum (FWHM):

$$R_{\text{E}} = \frac{2\sqrt{2\ln 2}\,\sigma_{E_\gamma}}{\mu_{E_\gamma}} \tag{3.13}$$

where μ and σ are the parameters resulting from the Gaussian fit (eq. (3.11)).

2025 JINST 20 P11016

In order to study the dependence of the energy resolution on the BP rate, we look into the relative change of the energy resolution when the BP rate in the detector is high (beam is present) with respect to the energy resolution when this rate is low (no beam):

$$\Delta R_{\mathrm{E}} = \frac{R_{\mathrm{E}}^{\mathrm{on}} - R_{\mathrm{E}}^{\mathrm{off}}}{R_{\mathrm{E}}^{\mathrm{off}}} \tag{3.14}$$

It is also useful to compare the count rate of the characteristic full energy peak, denoted by $\dot{N}_{E_\gamma}$ at high and low rates to provide a measurement of the loss of radioactive source events (e.g. due to unresolved pile-up). Analog to eq. (3.14), this relative change is defined as:

$$\Delta \dot{N}_{E_\gamma} = \frac{\dot{N}_{E_\gamma}^{\mathrm{on}} - \dot{N}_{E_\gamma}^{\mathrm{off}}}{\dot{N}_{E_\gamma}^{\mathrm{off}}} \tag{3.15}$$

3.7 Rise time

A fast signal rise time is convenient for distinguishing piled-up signals via the template matching algorithm. The rise time for each measurement is obtained from the corresponding template, that combines the information of different signals, regardless of their amplitude. For this experiment the rise time, denoted as t_{10-90}, is defined as the time difference between the 10 % and the 90 % of the maximum of the rising edge of the template.

3.8 Time resolution

A good timing resolution is advisable for the suppression of background caused by secondary particles [8]. An example in the clinical case would be γ-rays caused by neutron capture reactions on hydrogen. The time resolution of the system is defined as the spread in the difference between the interaction time of a BP in the detector and the 50 % of the rise time of the generated signal. Contributions to the time resolution are present along the whole signal generation process:

- Accelerator affects time resolution because of the intrinsic bunch time spread of the electrons in the accelerator (5 ps [13]) as well as the electronics to trigger on the radiofrequency reference signal (O_τ(100 ps) [21]).

- Intrinsic physical characteristics of the scintillation crystal introduce further time spread due to: 1) the intrinsic resolution of the $CeBr_3$ crystal during emission O_τ(100 ps [22]); 2) the additional spread due to the light bounces of this particular $\varnothing 1'' \times 1''$ geometry [23]; 3) the quality of the optical grease used for coupling and 4) the difference between the refraction index of the scintillator and the PMT that influences the number of scintillation photons transmitted to the PMT cathode [23]. These contributions dominate at lower energies because of the Poisson statistics of the scintillation light being produced: the higher the energy of the incident γ-ray, the more scintillation photons (and photoelectrons) emitted and thus the smaller the statistical contribution to the time resolution.

- The conversion and amplification in the PMT affect the system time resolution. In the selected PMT the manufacturer claims a quantum efficiency about 30 % for scintillation photons at 380 nm (limited fraction of photons are converted to electrons) with a time spread of ~190 ps

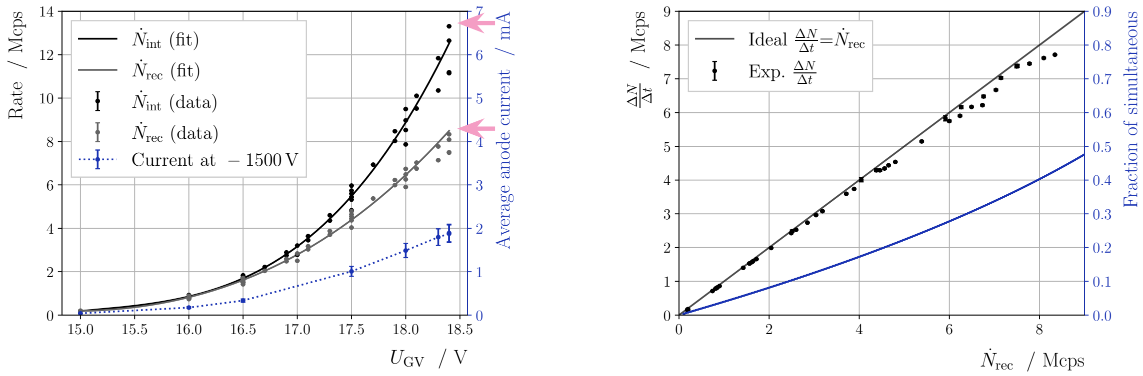

(a) Count rates $\dot{N}_{\rm int}$ (black) and $\dot{N}_{\rm rec}$ (gray) as a function of $U_{\rm GV}$. Only statistical errors are included in the error bars. Rounded markers indicate the data points, whereas solid lines are the corresponding to eq. (3.10). Blue points, referred to the blue right y-axis, indicate the average anode current (data at −1500 V), obtained as described in section 3.4. Dotted blue connecting segments are shown are shown as visual aid.

(b) Rounded markers: number of detected events N per unit time versus the recorded rate $\dot{N}_{\rm rec}$. The solid black line indicates the ideal case of perfect event deconvolution. The solid blue line (right y-axis) is the fraction of simultaneous events according to eq. (3.9).

Figure 4. Count rate of the $CeBr_3$ detector. The data correspond to datasets at different HVs ranging from −1000 to −1500 V.

FWHM for typical light pulses. Analog to the scintillation light production, also the Poisson statistics of the photoelectrons being amplified contribute.

The difference $t - t_{\mu b}$ is the time relative to the previous $T_{\mu b}$ period (eq. (3.2)). For a given energy, the spread of the distribution of this relative time defines the time resolution. To compute it, a 2D-histogram of the energy of the detected signals versus $t - t_{\mu b}$ is created (see figure 9) following the same methodology as [11]. For each energy bin, a 1D projection onto the abscissa axis is performed and the time resolution $R_{\rm T}$ is obtained as Gaussian fit (eq. (3.11) with $x \equiv t - t_{\mu b}$):

$$R_{\rm T} = 2\sqrt{2\ln 2}\,\sigma_{t-t_{\mu b}} \tag{3.16}$$

Considering the Poissonian nature of the production of scintillation photons, which is the dominating effect at low energies, the statistical fluctuation is proportional to inverse square root of the energy deposit. Thus, the dependence of the time resolution $R_{\rm T}$ on the energy E can be modeled as:

$$R_{\rm T}(E) = \frac{R_{\rm T}(1\,\mathrm{MeV})}{\sqrt{E/\mathrm{MeV}}} \tag{3.17}$$

4 Results

4.1 Bremsstrahlung photon rate estimation

The BP rate is estimated as explained in section 3.3. In figure 4(a), both $\dot{N}_{\rm int}$ and $\dot{N}_{\rm rec}$ are shown, together with the current flowing through the PMT anode (blue points referring to the right vertical axis).

As indicated with pink arrows, the maximal recorded count rate rises up to $\dot{N}_{\text{rec}} = (8.4 \pm 0.4)$ Mcps with a corresponding interacting rate $\dot{N}_{\text{int}} = (13.5 \pm 1.3)$ Mcps.

$\dot{N}_{\text{int}}$ is obtained from fitting the data to eq. (3.4). Multiple fits over different time intervals between $2T_{\mu\text{b}}$ to $2\,\mu$s ($26T_{\mu\text{b}}$) are performed to assess the robustness of $\dot{N}_{\text{int}}$ to the choice of fitting range. Excluding the first $T_{\mu\text{b}}$ period ensures $\dot{N}_{\text{int}}$ to be insensitive to the loss of events caused by the selected template length. In figure 4(a) only statistical errors are included in the error bars. Systematic errors due to the choice of the fit range starting point are below 12 % at low and medium gate voltages and range between 4 and 16 % for $U_{\text{GV}} \geq 18$ V.

In addition, a fit according to eq. (3.10) is performed in order to quantify the relationship between U_{GV} and the BP rate. The obtained parameters and the reduced χ_r^2 are shown in table 2.

Table 2. Fit parameters for $\dot{N}_{\text{int}}$ and $\dot{N}_{\text{rec}}$ to U_{GV} to function 3.10.

	a/Mcps	b/Mcps/V	c/Mcps/V^2	d/Mcps/V^3	χ_r^2
$\dot{N}_{\text{int}}$	-1030 ± 100	203 ± 18	-13.4 ± 1.1	0.297 ± 0.023	2.1
$\dot{N}_{\text{rec}}$	-110 ± 60	29 ± 11	-2.4 ± 0.7	0.063 ± 0.015	2.3

In figure 4(b), the number of detected events N per unit time versus the recorded rate $\dot{N}_{\text{rec}}$ inferred from $\dot{N}_{\text{int}}$ (eq. (3.8)) is depicted. This number of detected events is slightly smaller than $\dot{N}_{\text{rec}}$ because of the loss of events due to incorrect pile-up deconvolution, and the discrepancies intensify with increasing BP rates.

It's worth noting that, in a clinical setting (table 1), the micro-bunch repetition rate is eight times higher than at ELBE. Assuming the same interacting rate $\dot{N}_{\text{int}} \sim 10$ Mcps, the recorded rate (eq. (3.8)) will be 95 % of $\dot{N}_{\text{int}}$ rather than 70 % as in ELBE. This implies also a challenge since pile-up pulses from neighboring micro-bunches (separated 9.4 ns) need to be correctly deconvolved.

4.2 Anode current

The performance of the detector as a function of the BP rate is studied to inquire which detector configuration performs better at extremely high particle rates in such a broad energy range.

As shown in 4(a), the average anode current at a HV of -1500 V when the beam is on ($U_{\text{GV}} = 18.4$ V) reaches a maximum of 2 mA. This value is twenty times higher than the (long-term) maximum rating of the deployed PMT. The average current decreases exponentially when the PMT HV voltage is reduced, as well as when the accelerator U_{GV} is reduced.

Transient effects in the PMT anode current are also visible in figure 5(a)-top, namely when the beam is switched on, as explained below.

4.3 Gain and baseline drifts

Increasing the current through the PMT causes instabilities in the detector gain. This is shown in figure 5(a)-bottom, where the blue-yellow colored points indicate the energy deposit in the detector of the γ-rays emitted by the radioactive source and the contribution of the $_{\text{dark}}$BPs (more details in figure 9). The yellow line indicates the photoabsorption peak corresponding to the characteristic emission of the radioactive source (^{137}Cs). Its position plummets at 0.7 s, just when the system current increases because of the beam start. This is also observed in figure 5(a)-top, where the anode current flowing through the PMT is depicted. Both the calculated anode current from the recorded data (solid line) and the current supplied by the HV power supply (squared points) are shown. The monitor of the current supplied by the HV has a limited sampling rate of 1 Hz in this experiment and thus only 3 data points are included.

The decrease in the signal amplitude upon beam initiation is due to the sudden increase in PMT current demand. It temporarily exceeds the HV power supply's capacity causing a drop in the voltage of the dynodes and thus on the PMT gain. Within a few hundred milliseconds, the HV power supply, aided by the custom active base, adjusts to the higher current demand and restores the gain to its nominal level, as illustrated in figures 5(a) top and bottom.

In figure 5(b), the energy spectra before and during the beam are shown. The latter includes a time filter to exclude the BPs based on eq. (3.2). The gain drift observed in figure 5(a)-bottom corresponds to the change of the peak position of the spectrum during beam (blue) with respect to the spectrum before beam (gray), as indicated with pink arrows. The vertical shift illustrates the limitation of the signal processing algorithm. To identify signals piled-up within one $f_{\mu b}$ period, whose probability of occurrence increase with the BP rate, a smaller template length would be advisable.

The average gain drifts according to eq. (3.12) are shown in figure 6 for different HVs and CBs. Major differences among them are not determined by the HV, but by the shaping electronics. The configuration with CB1 at -1400 and -1500 V is the one that preserves better signal stability at increasing BP rates.

These data indicate that the calibration of the raw ADC counts (amplitude) to energy using a reference measurement with a radioactive source (and a given CB and HV) is not robust, since it does not account for the aforementioned dynamic gain variations.

Besides, we also observed dynamic variations of the offset of the digitized signal when looking at individual pulses (figure 3). On average, the baseline decreases when the BP rate in the detector increases and it slowly recovers (few hundreds ns, depending on the pulse load, see figure 3) when no more interactions occur. In the worst case, the baseline drift is 60 mV over a 1700 mV range (less than 4 % of the ADC dynamic range), and can lead to underflow (clipping). This is mostly HV independent, and is caused by an increasing current in the CB. Short-term baseline variations (within a pulse) distort the event identification and amplitude reconstruction, since the correlation between pulse shape and the template diminishes. On the other hand, the measured amplitude of the oscillating baseline noise was ~9 mV with all CBs, six times higher compared to the ~1.5 mV baseline noise obtained in previous characterizations without any CB.

4.4 Energy resolution

The configuration that better performs in terms of signal stability is CB1 at -1400 and -1500 V, meaning small gain drifts (according to figure 6, between -4 % and 12 %, depending on the incoming BP rate). Since we anticipated a better time resolution at -1500 V than at -1400 V, we consequently acquired more measurements with the former voltage. Therefore, energy resolution is studied only for setups at -1500 V.

Figure 7 compares measured spectra with Monte Carlo simulations based on low-count-rate experimental spectra (where sum events are negligible), incorporating both sum events and gain drifts. At higher incoming BP rates, the probability of detecting sum events increases, shifting the mean of the energy spectrum toward higher energies, as observed in [24].

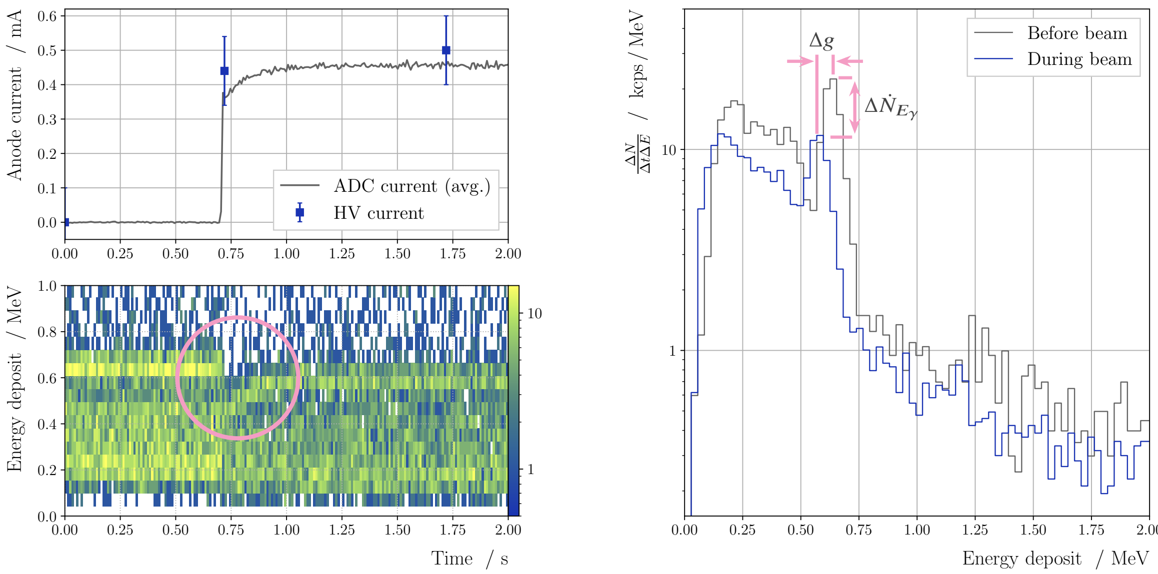

(a) Top: average PMT anode current (bin width = 0.028 s) derived from the digitized data (solid line) and from the HV supply monitor (square points) versus measurement time. Bottom: energy deposit versus measurement time (time bin width = 0.01 s, energy bin width = 0.057 MeV). The transient region (about 400 ms) with acute gain variability is highlighted with a pink circle. After it, the gain stabilizes at a slightly lower value than before the beam.

(b) Energy deposit spectrum before the beam starts (gray) and during irradiation (blue), the latter including only events out of synchrony with the electron beam (bin width = 0.028 MeV). The gain drop leads to a horizontal shift and a widening of the full energy peak. Likewise, the ^{137}Cs detected rate decreases notably (vertical shift), cf. section 3.3.

Figure 5. Measurement with the $CeBr_3$ detector, a radioactive ^{137}Cs source (662 keV characteristic emission) and the ELBE beam starting at 0.7 s. The operating voltage was -1000 V (CB3), and the count rates $\dot{N}_{\mathrm{int}} = (3.20 \pm 0.08)$ Mcps (fit) and $\dot{N}_{\mathrm{rec}} = (2.84 \pm 0.06)$ Mcps. The bias in the energy histograms results from the change of the calibrated signal amplitudes due to gain drifts.

The discrepancies between simulated and measured spectra become larger with increasing BP rate, and the main differences are observed in the spectra tails, at energies higher than 8 MeV. This effect can be caused by the lower efficiency for the absorption process of high-energy BPs in the scintillation crystal (neglected in the simulation), or by higher instabilities in the electron multiplication process due to the increase of the current through the PMT resulting from the higher number of scintillation photons produced in the cerium bromide. Also, the loss of some events due to the chosen template length choice may contribute to these discrepancies.

Energy resolution R_{E} and the relative difference ΔR_{E} are calculated as explained in section 3.6 (eq. (3.13) and eq. (3.14)). The results for measurements at -1500 V with CB1 are shown in figure 8. Figure 8(a) shows a constant energy resolution in the absence of beam (low rates, dashed lines). When the beam is present, the energy resolution worsens approx. proportionally to the BP rate (figure 8(b)). Note that the "beam off" data correspond to the datasets with the indicated $\dot{N}_{\mathrm{int}}$ but taken prior to beam initiation (in the absence of beam, the interacting rate in the detector remains

2025 JINST 20 P11016

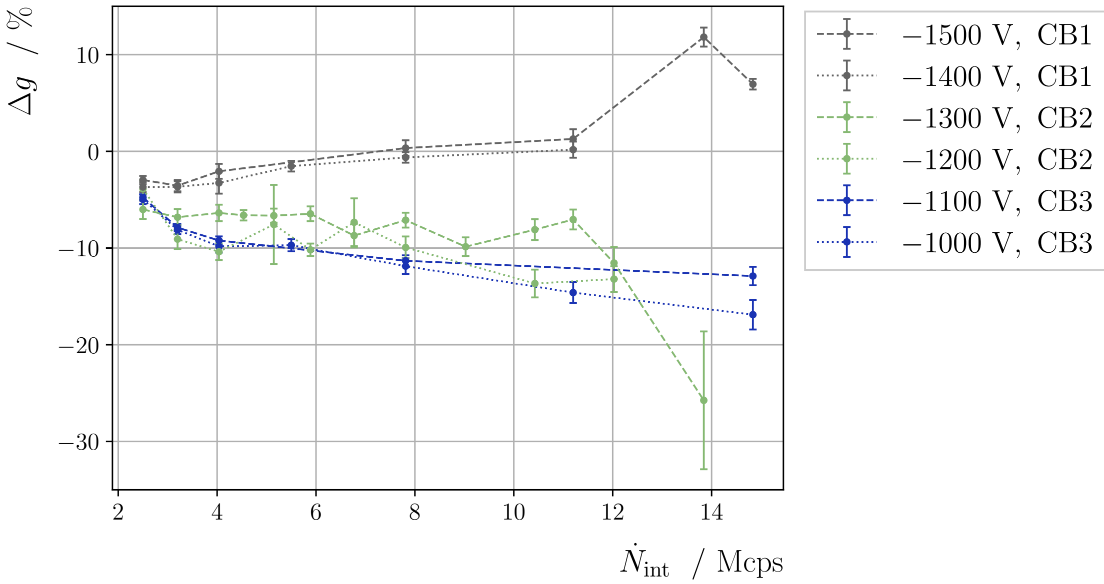

Figure 6. Gain drift versus BP interacting rate for all considered HVs. Blue for data with CB3, green for CB2 and gray for CB1, with dashed lines designating the highest HV for each CB and dotted lines for the lowest HV.

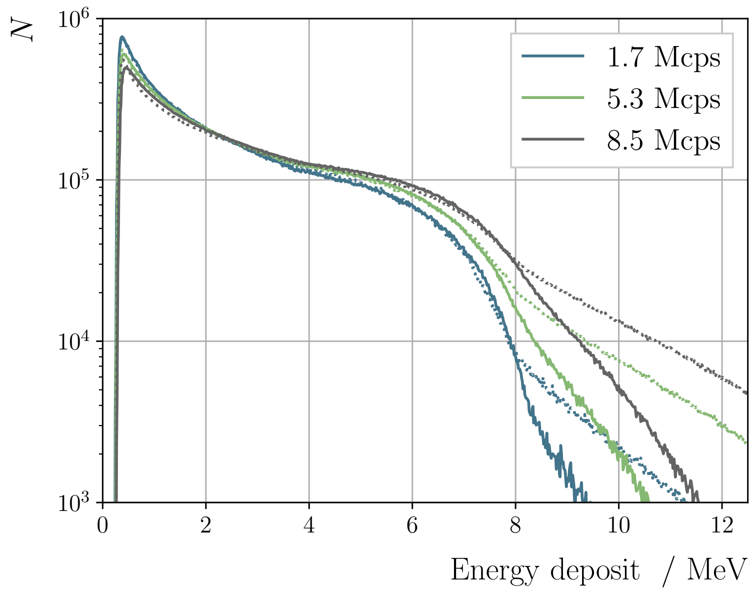

Figure 7. Comparison of experimental spectra (solid lines) at −1500 V (CB1) and the corresponding simulated spectra (dotted lines) at $\dot{N}_{\mathrm{int}}$ = 1.7 Mcps (blue), 5.3 Mcps (green) and 8.5 Mcps (gray). Binning of 0.012 MeV.

in the kcps order of magnitude). Compared to the results reported in [15], the obtained energy resolution is less favorable because the selected PMT together with the ADC dynamic range are not optimized in terms of energy resolution.

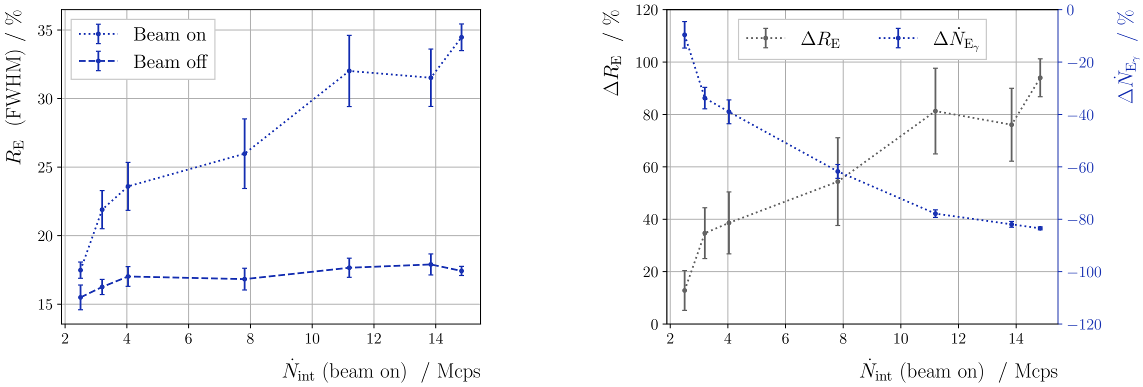

(a) Energy resolution (FWHM) according to eq. (3.13) before the beam is present (beam off, low rates, dashed line) and when the beam is present (beam on, high rates, dotted line), as a function of the interacting rate when the beam is on ($\dot{N}_{int}$).

(b) Relative change of the energy resolution (gray) according to eq. (3.14), and relative change of the characteristic emission rate (blue, referred to right y-axis) according to eq. (3.15), for the data in (a).

Figure 8. Energy measurements of the 662 keV photopeak (^{137}Cs) with the $CeBr_3$ detector at a HV of −1500 V (CB1), before and during the beam. The latter includes only events out of synchrony with the ELBE micro-bunches. Dotted and dashed segments are shown as visual aid.

As mentioned above, the amplitude reconstruction algorithm and thus the energy resolution is worse in case of pile-up events or transient baseline variations. Likewise, dynamic gain drifts within the beam, e.g. during the recovery period (see figure 5(a)) lasting up to 20 % of the beam period, tend to smear out the no longer Gaussian peak and worsen the signal-to-noise ratio (SNR) of the histogram to be fitted. The worsening in energy resolution could also be magnified due to the simple fitting procedure without background subtraction of $_{\text{dark}}$BPs.

Finally, the relative change of the rate of the characteristic photoemission $\Delta\dot{N}_{E_\gamma}$ according to eq. (3.15) is depicted also in figure 8(b) (right vertical axis). The discrepancies between the measured rate in the full energy peak before and during the beam escalate with increasing BP rate because of the higher probability of event loss due to pile-up events not being correctly deconvolved for the chosen template length.

4.5 Rise time

Measurements conducted in earlier laboratory tests without CB at HVs from −900 to −1500 V show a signal rise time t_{10-90} at 511 keV between 3 and 4 ns. The corresponding values when deploying CBs are listed in table 3 for different voltages. We verified that these values (and the normalized signal shape) was independent of the incoming BP rate, which is desirable for the proton therapy application.

The comparison of these results with the previous measurements without CB denote that the rise time is completely dominated by the CB (in all cases it is higher than the maximal value of 4 ns reported without CB), instead of being highly determined by the HV.

Finally, the measured decay constant with all CBs is between 25 and 30 ns at all considered HVs, compatible with the 25 ns reported in [15].

Table 3. Rise time t_{10-90} (10 % to 90 %) at each HV obtained as explained in section 3.7. Given t_{10-90} are the averages of the individual rise times at different incident BP rates.

	CB3		CB2		CB1	
HV/V	−1000	−1100	−1200	−1300	−1400	−1500
$\boldsymbol{t_{10-90}}$**/ns**	7.34 ± 0.11	7.44 ± 0.11	6.20 ± 0.10	6.20 ± 0.10	4.15 ± 0.11	4.10 ± 0.10

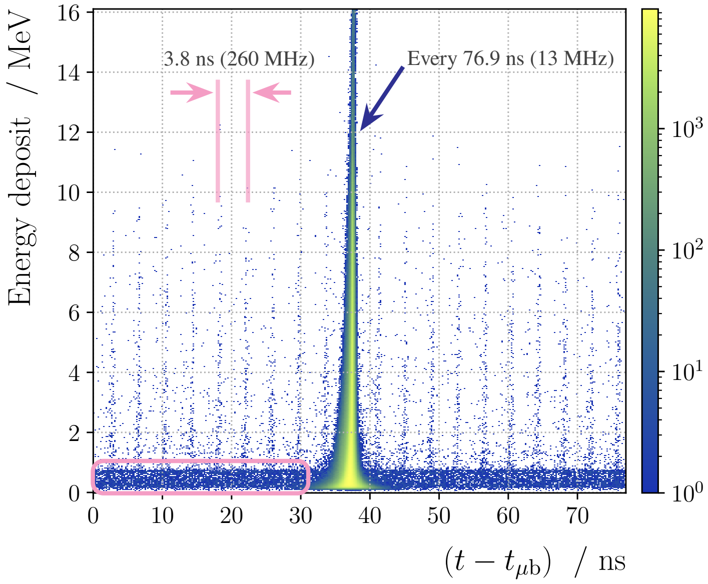

Figure 9. Energy deposit at the $CeBr_3$ detector versus relative time $t - t_{\mu b}$. The BPs are grouped in the central structure of the image (blue arrow), while the subsequent and less intense pattern (pink arrows) stem from ${}_{\text{dark}}$BPs. Besides, the blue-colored area below 1 MeV (pink rectangle) corresponds to γ-rays emitted by the radioactive source (not correlated with the repetition rate $f_{\mu b}$). The color scale indicates the number of events for a binning of 0.2 ns in the abscissas and 0.03 MeV in the ordinates axis. The measurement was performed with the PMT at −1000 V (CB3) and $\dot{N}_{\text{int}} \sim 3$ Mcps.

4.6 Time resolution

The time resolution is studied as explained in section 3.8. As an example, the 2D-histogram of the energy of the detected events versus the relative time $t - t_{\mu b}$ for one dataset at −1000 V and with an interacting rate ~3 Mcps is given in figure 9.

In figure 9, we see a dominant contribution of the BPs (arriving every 13 MHz or 76.9 ns) and a minor harmonic contribution at 260 MHz (3.8 ns). The homogeneous contribution at energies below 1 MeV corresponds to the γ-rays from the radioactive source (not correlated with $f_{\mu b}$).

Table 4. Fit parameter $R_{\text{T}}(1\,\text{MeV})$ for the time resolution according to eq. (3.17) for different HVs.

HV/V	−1000	−1100	−1200	−1300	−1400	−1500
$\boldsymbol{R_{\text{T}}}$**/ns**	0.841 11(6)	0.778 19(6)	0.760 83(4)	0.704 18(4)	0.545 91(2)	0.469 71(2)

2025 JINST 20 P11016

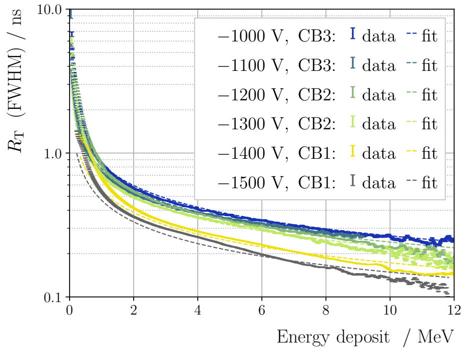

(a) Time resolution (data with error bars) at $\dot{N}_{\mathrm{int}} = 1.7$ Mcps ($\dot{N}_{\mathrm{rec}} = 1.6$ Mcps) and fits according to eq. (3.17) (dashed lines). Resulting fit parameters are summarized in table 4.

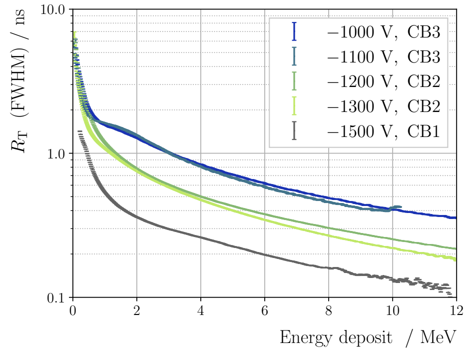

(b) Time resolution for different HVs at the measurement with counting rate closest to $\dot{N}_{\mathrm{int}} = 12.6$ Mcps ($\dot{N}_{\mathrm{rec}} = 8.1$ Mcps). No data available at −1400 V close to that count rate.

Figure 10. Time resolution (see section 3.8) versus energy deposit in the $CeBr_3$ detector.

Figure 10 discloses the time resolution for different HVs at low (figure 10(a)) and high (figure 10(b)) BP fluxes. Fits according to eq. (3.17) are performed for the former, and resulting fit parameters are given in table 4.

The higher the HV (in absolute value), the better the behavior of the time resolution, specially at high BP rates. For HVs of −1000 V and −1100 V CB3 is used, and this is the case with the highest time resolution variation with the incoming BP rate. The time resolution also worsens with the incident event rate for configurations with CB2 (−1200 V and −1300 V). Finally, at −1500 V (CB1) the smallest dependence on the incident BP rate and the best FWHM are achieved.

Figure 10(b) also reveals the strong dependence of the detector performance on the CB at high particle fluences. Once again, CB1 outperforms the rest of CBs. The time resolution of the crystal coupled with the PMT but without any CB has not yet been determined.

5 Discussion and conclusion

In this work, the results of the first stress tests of the proposed detector under extreme high BP fluences are presented. The motivation of this evaluation is to inquire whether the proposed $CeBr_3$ + PMT detector is suitable for its operation in clinical proton therapy irradiations, where it is well established that such device would need to cope with a count rate in the Mcps range [4, 10]. In this first experiment, the detector is placed directly in front of a bremsstrahlung beam in the γELBE facility, and the energy spectrum of the bremsstrahlung photons covers the same energy range as the one expected in the clinical setting. However, the bremsstrahlung beam has a continuous energy spectrum and its micro-bunch timing structure differs from the clinical case (see table 1).

To this purpose, the detector was irradiated at different bremsstrahlung fluxes, achieving recorded rates greater than 8 Mcps, with corresponding interacting rates greater than 12 Mcps (see figure 4(a)). This sets a new benchmark in the count rate of detected photons with a continuous energy spectrum up to 12.5 MeV that a detector based on a commercial scintillator crystal and PMT can sustain [4, 6, 10, 24].

2025 JINST 20 P11016

This success is based on the fully active voltage divider specifically developed for this work, together with the dead-time-free data acquisition system being used.

In the clinical proton therapy setting, a time resolution better than the typical time spread (about 2 ns, including proton bunch spread and proton transit times) is required [24] to distinguish prompt γ-rays (above 3 MeV) from other background sources. Our system fulfills this requirement showing an excellent sub-nanosecond time resolution for all considered HVs and incident BP fluxes at the energy range of interest. A time resolution around 200 ps FWHM was achieved with CB1 at -1400 and -1500 V at moderate rates and at -1500 V also at interacting rates greater than 12 Mcps (see figure 10). These values are in the same order of magnitude than the ones reported in [24, 25] for the U100 device at low to moderate count rates (lower than 3 Mcps).

Regarding energy resolution, it ranges from 15 to 35 % at -1500 V depending on the incident BP flux. These values are not as good as the values reported in [24] using a bigger scintillator crystal and a larger PMT. The modest values obtained with our detector are in part due to the small crystal size and in part to the PMT choice, motivated by its fast rise time and transit time spread, but not optimized for energy resolution. The dependence of the energy resolution on the incident rate is not desirable, but this can be further improved with refinements in the pile-up decomposition method. Moreover, removing the CB could also improve it since better signal shape, more baseline stability and less electronic noise is expected. At high BP fluences, the spectra measured with the presented detector shift toward higher energies due to the presence of sum events, consistent with the results reported in [24].

With regard to the analysis method, the template-based deconvolution algorithm efficiency and the quality of the energy reconstruction for piled-up signals is determined by the selected template length. This choice can be further optimized, together with the covariance threshold, to improve the outcome in terms of energy resolution and event identification. These weaknesses have lead to a worse BP rate determination and improving them would help in the study of the detector linearity.

The pulse shape characteristics of the produced signals have also been studied. In light of the outcome, the CB is the electronic component that most determines the signal shape. The first evidence is the strong dependence of the rise time on the CB rather than in the HV supplied. In addition, the time resolution at high BP fluences shows a stronger dependence on the CB rather than in the HV. Furthermore, baseline drifts related to the instabilities in the CB have been identified as well, and an increase in a factor 6 in the baseline noise when coupling the CB to the system has been reported. For all these reasons, we aim to remove the CB in future developments to eliminate undesirable effects in pulse shape and baseline stability. Removing the CB also enables a potential improvement on the signal rise time. However, without it, other strategies to protect the ADC must be studied. One possible solution is the reduction of the HV in order to ensure that the high load signals do not damage it, but this has a cost in terms of harnessing the ADC's full dynamic range.

Gain drift effects at sudden current increases have been identified (see figure 5(a)) and attributed to instabilities in the HV power supply. The inclusion of a large capacitor between the power supply and the PMT is envisioned as a possible way to solve this issue. Besides, no long-term deterioration in PMT output was found except instabilities that recover in short times (few hundreds milliseconds, see figure 5(a)).

As a result of all encountered instabilities, a robust accurate energy calibration between signal amplitude and energy was not possible, but this has not been a critical obstacle for the present study. Nevertheless, several actions are being studied to improve it in the future.

With the present results, it is not possible to conclude whether the detector maintains its linear behavior with increasing incident particle fluence or if it suffers from saturation because of the lack of information due to the faulty filtering of the auxiliary counter signals from the reference plastic detector.

Summarizing, the goal of this experiment was to determine whether the detector and its electronics (in its various configurations) are suitable to operate in environments with high γ-ray fluxes. We conclude that a good performance of the detector in the clinical setting is guaranteed, both in terms of incident BP flux and time resolution, in its actual configuration. Furthermore, improvement potentials in the electronics and the analysis method have been identified. Overall, this encourages further investigations of the coaxial prompt γ-ray method, and an upcoming experiment in a more realistic scenario: a clinical proton therapy accelerator using homogeneous phantoms at relevant doses and beam currents.

Acknowledgments

This work has been supported by Xunta de Galicia, Spain, under the Industrial Doctorates Program 2022 (Galician Innovation Agency) and under grant number ED431C/3, by Ministerio de Ciencia e Innovación, Spain, under project PID2022-140591NB-I00 and by Generalitat Valenciana, Spain, (Conselleria de Educación, Investigación, Cultura y Deporte) under grant number CDEIGENT/2019/011. This work has also received funds from the Particle Therapy Cooperative Group (PTCOG) under project funding 2024 and from the European Union's 2020 research and innovation program under grant 101008126, corresponding to RADNEXT project. IGFAE is supported by the María de Maeztu grant CEX2023-001318-M and IFIC by the Severo Ochoa Center of Excellence grant CEX2023-001292-S, both funded by MCIU/AEI.

We like to thank D. Calvo, J. Casaña-Copado, J. Collado, A. Delgado, A. Dreyer, D. Esperante, A. Ferrari, L. M. Fraile, T. Fritzke, A. Gallas-Torreira, C. García, B. Gimeno, D. Ginestar, C. Golnik, B. Gorissen, T. Häupke, J. L. Hueso, G. Kasprowitz, M. Kirsch, E. Lemos Cid, G. Llosá, P. Martín-Luna, R. Montañana, E. Nácher, G. Pausch, A. Pazos Álvarez, E. Pérez Trigo, J. Petzoldt, D. Real, J. Riera, A. Ros, J. Roser, H. Schulz, C. Senra, J. Serrano, N. Shusharina, J. Stein, J. L. Taín, J. M. Udías, E. van der Bij, R. Viegas and A. Wagner for useful discussions and their help, as well as the informatics, electronics, mechanics, transfer & innovation and management departments at IFIC and IGFAE, the support of the TripleAlpha team with a special mention to A. Dosil, and the open-source community, ROOT and KiCad developers for their support. We warmly thank the ELBE accelerator crew for stable operations and their constant support during the beamtime.

Data Availability Statement. This article has associated data in a data repository. The experimental raw data analyzed in this article are freely available to download at https://doi.org/10.14278/rodare.2807 [26].

References

[1] A.-C. Knopf and A. Lomax, *In vivoproton range verification: a review*, Phys. Med. Biol. **58** (2013) R131.

[2] K. Skjerdal et al., *Range verification in proton therapy with computational prompt gamma-ray spectroscopy: A Monte Carlo study*, Radiat. Phys. Chem. **238** (2026) 113096.

2025 JINST 20 P11016

[3] S. Bertschi et al., *Potential margin reduction in prostate cancer proton therapy with prompt gamma imaging for online treatment verification*, *Physics and Imaging in Radiat. Oncol.* **26** (2023) 100447.

[4] T. Werner et al., *Processing of prompt gamma-ray timing data for proton range measurements at a clinical beam delivery*, *Phys. Med. Biol.* **64** (2019) 105023.

[5] C. Richter et al., *First clinical application of a prompt gamma based in vivo proton range verification system*, *Radiotherapy and Oncology* **118** (2016) 232.

[6] F. Hueso-González et al., *A full-scale clinical prototype for proton range verification using prompt gamma-ray spectroscopy*, *Phys. Med. Biol.* **63** (2018) 185019.

[7] J. Berthold et al., *First-In-Human Validation of CT-Based Proton Range Prediction Using Prompt Gamma Imaging in Prostate Cancer Treatments*, *Int. J. Radiat. Oncol. Biol. Phys.* **111** (2021) 1033.

[8] F. Hueso-González et al., *Compton Camera and Prompt Gamma Ray Timing: Two Methods for In Vivo Range Assessment in Proton Therapy*, *Front. Oncol.* **6** (2016) 80.

[9] F. Hueso-Gonzalez and T. Bortfeld, *Compact Method for Proton Range Verification Based on Coaxial Prompt Gamma-Ray Monitoring: A Theoretical Study*, *IEEE Trans. Radiat. Plasma Med. Sci.* **4** (2020) 170.

[10] G. Pausch et al., *Detection systems for range monitoring in proton therapy: Needs and challenges*, *Nucl. Instrum. Meth. A* **954** (2020) 161227.

[11] K. Römer et al., *Characterization of scintillator crystals for usage as prompt gamma monitors in particle therapy*, 2015 *JINST* **10** P10033.

[12] F. Miguéis et al., *Sensitivity of coaxial prompt gamma-ray monitoring in heterogeneous geometries: A Monte Carlo simulation study*, *Radiat. Phys. Chem.* **232** (2025) 112639.

[13] R. Schwengner et al., *The photon-scattering facility at the superconducting electron accelerator ELBE*, *Nucl. Instrum. Meth. A* **555** (2005) 211.

[14] F. Hueso-González et al., *A dead-time-free data acquisition system for prompt gamma-ray measurements during proton therapy treatments*, *Nucl. Instrum. Meth. A* **1033** (2022) 166701.

[15] F.G.A. Quarati et al., *Scintillation and detection characteristics of high-sensitivity CeBr3 gamma-ray spectrometers*, *Nucl. Instrum. Meth. A* **729** (2013) 596.

[16] A.F. Prieto et al., *PMT System for Prompt Gamma-ray Measurements during Proton Therapy Treatments*, in the proceedings of the *IEEE Nuclear Science Symposium and Medical Imaging Conference*, Online, Italy, November 5–12 (2022) [`DOI:10.1109/nss/mic44845.2022.10399096`].

[17] J. Petzoldt et al., *Characterization of the microbunch time structure of proton pencil beams at a clinical treatment facility*, *Phys. Med. Biol.* **61** (2016) 2432.

[18] F. Hueso-González et al., *First test of the prompt gamma ray timing method with heterogeneous targets at a clinical proton therapy facility*, *Phys. Med. Biol.* **60** (2015) 6247.

[19] A. Ferreira et al., *GAN-based generation of realistic 3D volumetric data: A systematic review and taxonomy*, *Med. Image Anal.* **93** (2024) 103100.

[20] G. Knoll, *Radiation Detection and Measurement (4th ed.)*, John Wiley, Hoboken, NJ (2010).

[21] F. Hueso-González, *Nuclear methods for real-time range verification in proton therapy based on prompt gamma-ray imaging*, Ph.D thesis, Technische Universität Dresden, Dresden, Germany (2016), `http://nbn-resolving.de/urn:nbn:de:bsz:14-qucosa-204988`.

[22] L.M. Fraile et al., *Fast timing study of a CeBr3 crystal: Time resolution below 120 ps at 60Co energies*, *Nucl. Instrum. Meth. A* **701** (2013) 235.

2025 JINST 20 P11016

[23] P. Lecoq, *New Approaches to Improve Timing Resolution in Scintillators*, *IEEE Trans. Nucl. Sci.* **59** (2012) 2313.

[24] G. Pausch et al., *Scintillator-Based High-Throughput Fast Timing Spectroscopy for Real-Time Range Verification in Particle Therapy*, *IEEE Trans. Nucl. Sci.* **63** (2016) 664.

[25] J. Petzoldt, *Toward the Clinical Application of the Prompt Gamma-Ray Timing Method for Range Verification in Proton Therapy*, Ph.D. thesis, Technische Universität Dresden, Dresden, Germany (2016), `https://tud.qucosa.de/en/api/qucosa.:30714/attachment/ATT-0/`.

[26] I. García Rivas et al., *High-count rate photon detection with scintillators coupled to photomultiplier tubes and fast digitizers* [`DOI:10.14278/rodare.2807`].